Direct numerical simulation of the flow around a rectangular cylinder at a moderately high Reynolds number / Cimarelli, Andrea; Leonforte, Adriano; Angeli, Diego. - In: JOURNAL OF WIND ENGINEERING AND INDUSTRIAL AERODYNAMICS. - ISSN 0167-6105. - 174:(2018), pp. 39-49. [10.1016/j.jweia.2017.12.020]

# Direct numerical simulation of the flow around a rectangular cylinder at a moderately high Reynolds number

Andrea Cimarelli*, Adriano Leonforte*, Diego Angeli*

*DISMI, University of Modena and Reggio Emilia, 42122, Reggio Emilia, Italy*

**Abstract**

We report a Direct Numerical Simulation (DNS) of the flow around a rectangular cylinder with a chord-to-thickness ratio $B/D = 5$ and Reynolds number $Re = 3000$. Global and single-point statistics are analysed with particular attention to those relevant for industrial applications such as the behaviour of the mean pressure coefficient and of its variance. The mean and turbulent flow is also assessed. Three main recirculating regions are found and their dimensions and turbulence levels are characterized. The analysis extends also to the asymptotic recovery of the equilibrium conditions for self-similarity in the fully developed wake. Finally, by means of two-point statistics, the main unsteadinesses and the strong anisotropy of the flow are highlighted. The overall aim is to shed light on the main physical mechanisms driving the complex behaviour of separating and reattaching flows. Furthermore, we provide well-converged statistics not affected by turbulence modelling and mesh resolution issues. Hence, the present results can also be used to quantify the influence of numerical and modelling inaccuracies on relevant statistics for the applications.

*Keywords:* Flow benchmark; Rectangular cylinder; Flow reattachment; Direct Numerical Simulation;

*Corresponding author

*Email address:* andrea.cimarelli@unimore.it (Andrea Cimarelli)

*Preprint submitted to Journal of Wind Engineering and Industrial Aerodynamics December 11, 2017*

## 1. Introduction

The flow around bluff bodies with sharp corners is known to be of overwhelming interest for several wind engineering applications [1]. The case of a rectangular cylinder encompasses the range of bluff bodies from a flat plate normal to the flow, to a square cylinder, and, finally, to a flat plate parallel to the flow, as its chord-to-thickness ratio is varied from zero to infinity. For these reasons, these kind of flows have been the subject of several numerical and experimental studies. Of particular interest for civil engineering applications is the case of slender bodies typical of buildings and structures. A peculiarity of these shapes resides in the fact that the flow exhibits a large-scale separation at the leading-edge and also a reattachment before the definitive separation at the trailing-edge. Indeed, while the shedding instability in the wake is observed in all bluff bodies, only long bluff bodies present further instabilities which are due to the separating and reattaching leading-edge shear layer. This leads to the formation of an additional shedding of large-scale vortices before the trailing edge. A detailed investigation into the nature of this separating and reattaching flow is found in Cherry *et al.* [2]. Despite the fact that these kind of flows have been the subject of several numerical and experimental studies, the topic is still attractive, as highlighted in a recent work by Bruno *et al.* [3]. From an applicative point of view, the interest is given by the fact that both experimental and numerical techniques appear to be unable to tackle the problem in a unequivocal way. Indeed, a large variability of results is found in the literature, even for global or first order statistics, see again the review of Bruno *et al.* [3]. The reason of these discrepancies is the high sensitivity of the flow on the test boundary conditions and measurement accuracy in experiments and on the turbulence model, numerical schemes and mesh properties in CFD analysis. Here, we focus on the numerical approach.

For low Reynolds numbers, $10^2 < Re < 10^3$ where $Re = U_\infty D/\nu$, $U_\infty$ the free-stream velocity, $D$ the rectangular cylinder thickness and $\nu$ the kinematic viscosity, the flow around rectangular cylinders has been studied in several works, see e.g. Nakamura *et al.* [4], Ohya *et al.* [5], Hourigan *et al.* [6], and Tan *et al.* [7]. The main aim of the above mentioned works is the assessment of the main instabilities of the flow and of the self-sustaining mechanisms which generate them. Concerning the high Reynolds number regime, $Re > 10^4$, it is worth mentioning the works of Shimada and Ishihara [8] and of Yu and Kareem [9] where RANS (Reynolds Average Navier-Stokes) and LES (Large Eddy Simulation) techniques are respectively used. In this context, it is important to point out a benchmark activity on the aerodynamics of rectangular cylinders at Reynolds numbers of the order of $10^4$, i.e. the BARC project (Benchmark on the Aerodynamics of a Rectangular 5:1 Cylinder) [10]. Within this framework, a series of experiments and simulations have been conducted aiming at establishing reliable standards for the simulation and measurement of such a flow configuration, see e.g. Bruno *et al.* [11], Mannini *et al.* [12], Ricci *et al.* [13] and Patruno *et al.* [14] for its extension to non-null angles of attack.

As summarized in Bruno *et al.* [3], the recent results within the BARC project are still characterized by a large scatter, thus highlighting that a clear picture of the combined influence of mesh resolution, turbulence model and boundary conditions on the flow statistics is still missing. One of the possible reasons is that, up to now, no reference data are available in the literature, i.e. experimental data obtained under well-defined boundary conditions (e.g. free-stream turbulence level) and unaffected by measurement errors, or numerical data not influenced by modelling and mesh resolution issues. Indeed, to the best of the authors' knowledge, no Direct Numerical Simulation (DNS) for sufficiently high Reynolds number has been performed in such a flow configuration. We found only two attempts in the literature. In the first one, Tamura *et al.* [15] approached the problem by means of a finite difference technique at high Reynolds number, $Re = 10^4$. However, the grid resolution adopted was not fine enough to capture the smallest scales of motion and, hence, the simulation reported appears to be more an implicit LES than a DNS. More recently Hourigan *et al.* [6] proposed a more accurate analysis through a spectral-element method. However, the DNS data reported refer to very low Reynolds numbers, namely from $Re = 350$ to $Re = 500$, and a fully developed turbulent state is not achieved.

In the present work we produce, for the first time, high-fidelity data of the flow around a rectangular cylinder with chord-to-thickness ratio $B/D = 5$ and Reynolds number $Re = 3000$. The study is aimed at understanding the main physical mechanisms driving the flow and at providing statistics, not affected by numerical issues, to be used for the validation and calibration of CFD techniques. For obvious computational cost reasons, the Reynolds number considered, $Re = 3 \cdot 10^3$, is smaller than the ones considered in the recent literature. However, let us point out that as shown by Sasaki and Kiya [16], the flow develops the main turbulent structures typical of larger Reynolds numbers already for $Re > 380$. By further increasing $Re$, it is also found that the bubble length does not increase significantly anymore. It is also worth mentioning that, based on spectral arguments, Nakamura *et al.* [17] argue that an asymptotic large Reynolds number regime is attained for $Re = 3000$ since for $Re > 3000$ the Strouhal number of the spectral peak does not increase anymore. Based on these results, we argue that the considered Reynolds number is sufficiently large to capture the main physical features observed at larger Reynolds numbers. As an example, the two main unsteadinesses observed by Kiya and Sasaki [18, 19] for very large Reynolds numbers and consisting of a shedding of vortices from the separation bubble and of a large scale oscillation encompassing the entire flow field, are found to be reproduced both qualitatively and quantitatively at the present Reynolds number (see section §3 for the details).

The paper is organized as follows. A description of the numerical simulation and of the statistical procedure is reported in section §2. The main statistical properties of the flow, with particular attention to those mostly debated in the BARC project, are shown in section §3. In order to rigorously assess the physical features characterizing the flow, single-point and two-point statistics are analysed in detail in sections §4 and §5. The paper is then closed by final remarks in section §6.

## 2. Direct Numerical Simulation and statistical convergence

A Direct Numerical Simulation has been performed to study the flow around a rectangular cylinder. The evolution of the flow is governed by the continuity and momentum equations,

$$\begin{aligned} &\frac{\partial u_i}{\partial x_i} = 0 \\ &\frac{\partial u_i}{\partial t} + \frac{\partial u_i u_j}{\partial x_j} = -\frac{\partial p}{\partial x_i} + \frac{1}{Re}\frac{\partial^2 u_i}{\partial x_j x_j} \end{aligned} \qquad (1)$$

where $x = x_1$ $(u = u_1)$, $y = x_2$ $(v = u_2)$, $z = x_3$ $(w = u_3)$ are the streamwise, vertical and spanwise directions (velocity components), $p$ is the pressure field and $Re = U_\infty D/\nu$ is the Reynolds number where $U_\infty$ is the free-stream velocity, $D$ is the thickness of the rectangular cylinder and $\nu$ is the kinematic viscosity. In accordance with the above equations, all the variables presented in the following will be reported in a dimensionless form by using $D$ as length scale and $D/U_\infty$ as time scale. A cell-centered finite volume method has been chosen to discretize the equations by means of the OpenFOAM® open source code [20]. Time integration is performed by means of a second-order backward Euler implicit scheme while convective and diffusive fluxes at the volume faces are evaluated through a second-order central difference scheme. Finally, a pressure-implicit split-operator algorithm [21] is used to numerically solve the pressure-velocity coupling. Given the simple geometry of the problem, a block-structured Cartesian grid is adopted. Inlet-outlet boundary conditions are imposed in the streamwise direction. The inlet condition is a simple unperturbed flat velocity profile. The outlet boundary condition combines a Neumann/Dirichlet condition. In particular, a stress-free (zero gradient) condition is enforced when the flow exits the boundary, while a zero velocity vector is imposed when an inward flow is detected. The same kind of boundary condition is imposed in the vertical direction, the only difference being that in case of inward flow the imposed Dirichlet condition equals the free-stream inlet velocity. Finally, periodic conditions are imposed in the spanwise direction.

The flow case consists of a rectangular cylinder whose dimensions are $(L_x, L_y) =$

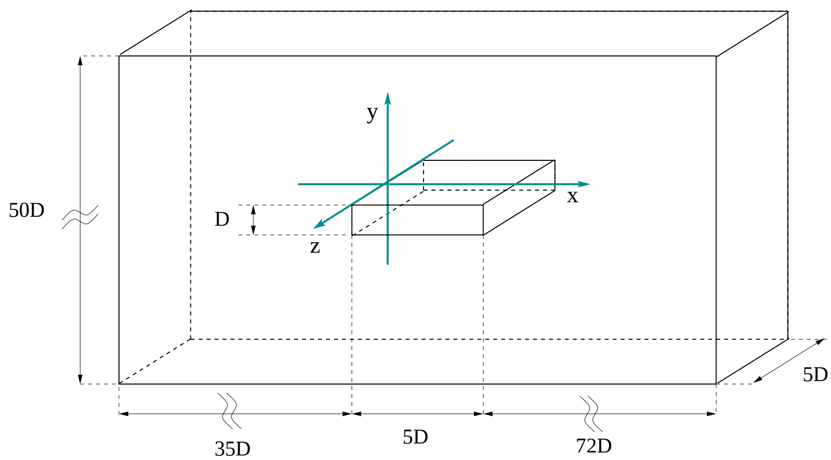


Figure 1: Configuration of the system.

$(5D, D)$. The Reynolds number considered is $Re = 3000$. The extent of the numerical domain is $(\mathcal{D}_x, \mathcal{D}_y, \mathcal{D}_z) = (112D, 50D, 5D)$ and is found large enough to not interfere with the flow dynamics, see the analysis of the spanwise correlation function shown in section §5. A sketch of the system configuration and of the reference coordinate system is reported in figure 1. The structured Cartesian grid employed is composed by $1.5 \cdot 10^7$ volumes. A multi block-structured approach is used by employing 5 main blocks characterized by a stepwise variation of the number of volumes in the spanwise direction. In particular, in the inner block, the number of volumes in the $(x, z)$-plane above the rectangle is $(Nx, Nz) = (128, 144)$ in the streamwise and spanwise direction, respectively. The volume distribution is homogeneous in the spanwise direction while in the streamwise and vertical directions a geometric progression is adopted, $\Delta x_i = k_x^{i-1} \Delta x_1$ and $\Delta y_j = k_y^{j-1} \Delta y_1$ with $k_x = 1.06$, $k_y = 1.04$, $\Delta x_1 = 0.004$ and $\Delta y_1 = 0.004$. This approach is used to obtain higher resolution levels in the near-wall leading- and trailing-edge regions. Such a practice leads to a mean wall resolution of $(\overline{\Delta x^+}, \overline{\Delta y^+}, \overline{\Delta z^+}) = (6.1, 0.31, 5.41)$, where $\overline{(\cdot)}$ denotes the streamwise average along the rectangle length and the superscript $+$ implies normalization with friction units. The time step varies during simulation to obtain a condition $CFL < 1$ in each point of the domain, the resulting average

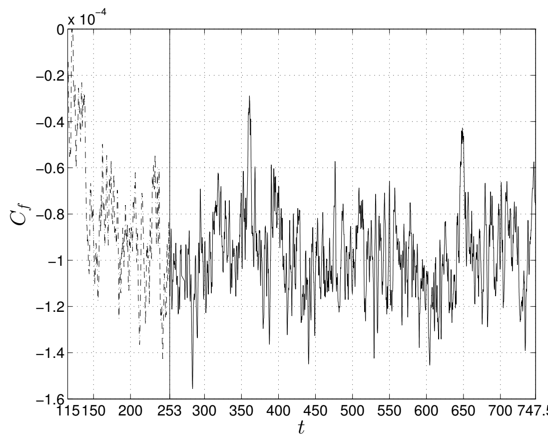


Figure 2: Time-behaviour of the friction drag coefficient $C_f$. The vertical line denotes the end of the initial transient and the start of the fully developed state used for the computation of the statistics. To note that the plot starts from $t = 115$. Indeed, from $t = 0$ to $t = 115$ a precursory coarser simulation has been used to reduce the computational time for reaching a flow state close to the statistical equilibrium.

time step being $\Delta t = 0.0023$.

In the present flow case, the computational demand for well-converged statistics denoted as $\langle \cdot \rangle$, is mitigated by the statistical stationarity of the flow field and by the statistical homogeneity in the spanwise direction. Furthermore, the flow exhibits certain statistical symmetries in the vertical direction which are better expressed by shifting the origin of the vertical coordinate to the centre of the prism, $\tilde{y} = y - D/2$. Indeed, the transformation $\tilde{y} \to -\tilde{y}$ leaves quantities like $U = \langle u \rangle$, $\langle u_i u_i \rangle$ statistically invariant while reversing the sign of quantities like $V = \langle v \rangle$, $\langle uv \rangle$ and $\partial \langle \cdot \rangle / \partial \tilde{y}$. In conclusion, the average of a generic quantity $\beta$ is defined as

$$\langle \beta \rangle (x, \tilde{y}) = \frac{1}{N} \sum_{i=1}^{N} \frac{1}{2} \left( \frac{1}{L_z} \int_{-L_z/2}^{L_z/2} \beta(x, \tilde{y}, z, t) dz \pm \frac{1}{L_z} \int_{-L_z/2}^{L_z/2} \beta(x, -\tilde{y}, z, t) dz \right) , \tag{2}$$

where the sum and difference of the two integrals is given by the symmetric or antisymmetric property of the considered variable, respectively. The number of fields sampled during time is $N = 317$. These samples are taken once the initial

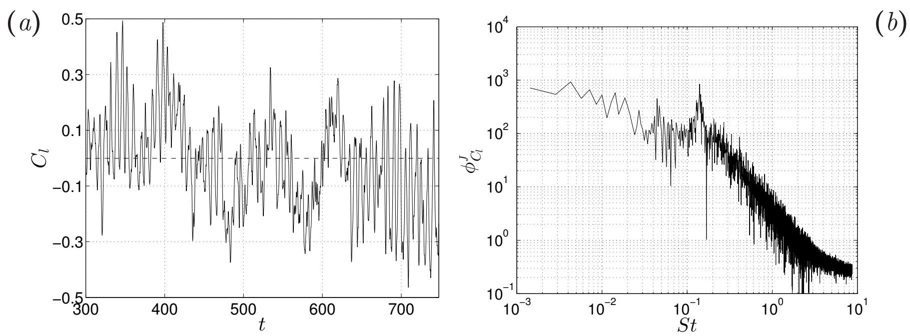


Figure 3: (a) Time evolution of the lift coefficient $C_l$. (b) Frequency spectrum of the lift coefficient, $\phi^f_{C_l}$, as a function of the Strouhal number $St$.

transition of the flow field is washed out, see figure 2, and are taken with a time separation $\Delta T = T$ where $T = D/U_\infty$ is the characteristic time scale of the flow. In the following, the customary Reynolds decomposition of the velocity field is adopted, $u_i = U_i + u'_i$, where $U_i$ and $u'_i$ denote the mean and fluctuating velocity.

## 3. Main properties of the flow

We start the analysis by considering the main integral parameters of the flow, i.e. the lift, $C_l$, and drag, $C_d$, coefficients. Obviously, for symmetry reasons, the average lift coefficient is null, $\widetilde{C_l} = 0$ where $\widetilde{\cdot}$ denotes the time average. As shown in figure 3(a), instantaneously the lift coefficient is not zero, but it fluctuates in time. Different time scales are recognized and can be studied by considering the frequency spectrum defined as

$$\phi^f_{C_l}(St) = \hat{C}_l \hat{C}_l^* \tag{3}$$

where $\hat{\cdot}$ denotes the Fourier transform, $^*$ the complex conjugate and $St$ the dimensionless frequency, i.e. the so-called Strouhal number. As shown in figure 3(b), the frequency spectrum confirms the presence of different temporal scales. In particular, a clear peak for $St \approx 0.14$ is present and will be shown in the following to be related with the frequency of the large scale vortex detachment

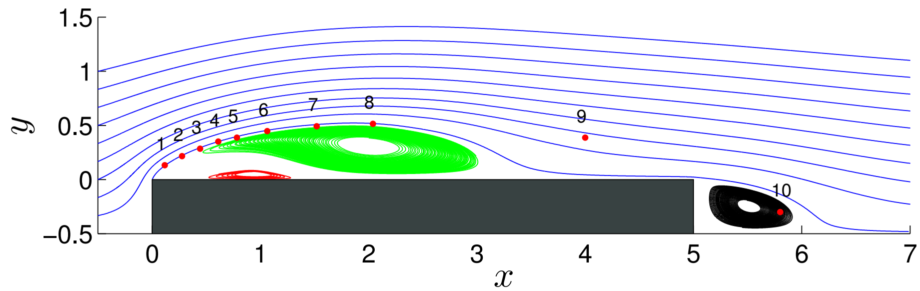


Figure 4: Streamlines of the mean velocity field $(U, V)(x, y)$. The green lines show the *primary vortex*, the red lines mark the *secondary vortex* and the black lines denote the *wake vortex*. The red dots denote the locations of the probes used for the computation of time spectra in section §5.

in the wake. A second peak is recognizable at a lower frequency, namely $St \approx 0.042$. This very low frequency is responsible for the long term fluctuations of $C_l$ observed in figure 3(a) and could explain the scatter of the data of $\widetilde{C}_l$ obtained in different works, see the review of Bruno *et al.* [3], as a result of statistical convergence problems. The frequencies of the two spectral peaks detected here quantitatively agree with those observed in Kiya and Sasaki [18, 19] for very large Reynolds numbers. In accordance with these works, we argue that the peak at $St \approx 0.14$ is related with a large scale shedding of vortices from the main recirculating region while the very slow peak at $St \approx 0.042$ is due to the presence of a low-frequency unsteadiness encompassing the entire flow field. Concerning the drag coefficient, we measure that $\widetilde{C}_d = 0.96$.

Let us now consider the topology of the mean flow field. As shown in figure 4, the streamlines of the mean flow highlight the presence of a large scale recirculation extending from the leading edge up to $x_r \approx 3.65$, see the green lines in figure 4. The centre of rotation, defined as the singularity point within the recirculating region where the mean velocity field vanishes $(U, V) = (0, 0)$, is located at $(x_c^{pv}, y_c^{pv}) = (2.04, 0.35)$. This separation bubble will be hereafter called the *primary vortex*. As shown by the isocontours of mean pressure in figure 5, this separated region is associated with a large area of low pressure with a mini-

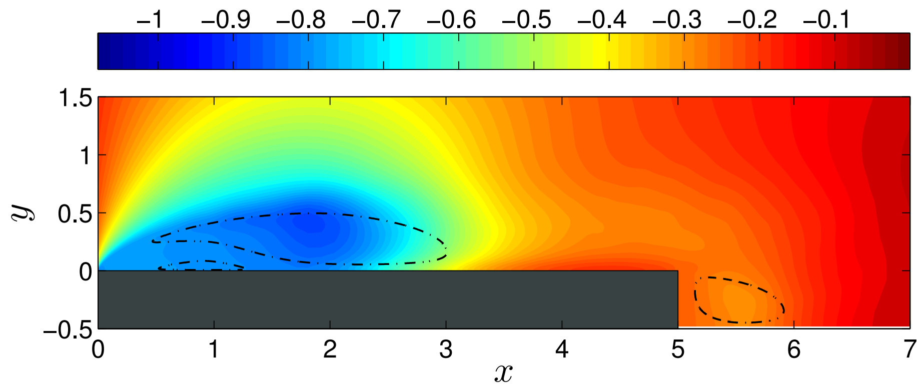


Figure 5: Isocontours of the mean pressure field $P(x, y)$. The dashed lines report the location of the *primary vortex*, *secondary vortex* and *wake vortex*.

mum located at $(x_p^{pv}, y_p^{pv}) = (1.81, 0.42)$. It is worth noting that the location of this minimum does not coincide with the centre of the *primary vortex*, thus highlighting the strongly inhomogeneous non-axisymmetric shape taken by the recirculating flow. Actually, a second recirculating region is present and highlighted with red lines in figure 4. This *secondary vortex* takes place below the *primary vortex*. Indeed, the reverse flow induced in the near-wall region by the *primary vortex* creates a boundary layer moving upstream. As shown by the isocontours of the mean pressure field in figure 5, the induced boundary layer undergoes an adverse pressure gradient, hence it decelerates, becomes thicker and, finally, breaks down leading to a further separation. Hence, the *secondary vortex*, being induced by the *primary vortex*, is counter-rotating with respect to the *primary vortex* and its characteristic length and time scales are smaller than those of the *primary vortex*. The *secondary vortex* is found to extend for $0.4 < x < 1.4$. The intensity of the mean flow within this region is very low, thus highlighting how this object is difficult to capture from a statistical point of view, see Bruno *et al.* [3] for a review of the different results in literature. After the reattachment point, for $x > x_r$, the flow evolves in a downstream boundary layer and finally detaches at the trailing edge where it develops into the wake. As shown with black lines in figure 4, the separated wake highlights a *wake vortex* extending from the trailing edge down to $x \approx 6.2$ and centered at $(x_c^{wv}, y_c^{wv}) = (5.5, -0.25)$. As for the *primary vortex*, the *wake vortex* sets a low pressure region centered at $(x_p^{wv}, y_p^{wv}) = (5.52, -0.27)$, see figure 5. The main difference with respect to the leading-edge recirculation is given by the fact that the extent and intensity of the low pressure area are smaller.

Let us now study the streamwise behaviour of the skin friction and pressure coefficients along the horizontal surface of the rectangular cylinder. As shown in figure 6(a), the mean skin friction coefficient $\langle c_f \rangle(x)$ exhibits strong negative values in the very first part of the rectangular cylinder, close to the leading-edge corner. Then, $\langle c_f \rangle$ increases and reaches small but positive values in the region $0.4 < x < 1.4$. This region of positive shear is the near-wall footprint of the *secondary vortex*. Moving downstream, for $1.4 < x < 3.65$, the average skin friction coefficient becomes negative again and shows a minimum at $x \approx 2.37$. This region of negative shear is the near-wall footprint of the *primary vortex*. Actually, the *primary vortex* is responsible also for the previously observed strong negative values of $\langle c_f \rangle(x)$ in the leading-edge region thus indicating that the *primary vortex* reattaches upstream the *secondary vortex*. Finally, in the last part of the rectangular cylinder, for $x > 3.65$, a forward attached boundary layer takes place. Indeed, the skin friction is positive and assumes increasingly large values moving downstream.

Let us now considering the streamwise behaviour of the pressure coefficient $\langle c_p \rangle(x)$ and of its variance $\langle c_p'^2 \rangle(x)$ shown in figure 6(b). These two observables are of paramount relevance for the applications since they carry information about the aerodynamic loads and their fluctuations. However, as pointed out in Bruno *et. al* [3], the prediction of these two statistical observables is very challenging for numerical simulations, as highlighted by the variability of the results obtained within the BARC project. The reason is that the behaviour of $\langle c_p \rangle(x)$ and $\langle c_p'^2 \rangle(x)$ is strongly influenced by the shape and extent of the re-circulating regions of the flow, which in turn are determined by the turbulence levels therein. Hence, the turbulence modelling and mesh resolution adopted in numerical simulations strongly impacts the resolved turbulent dynamics and,

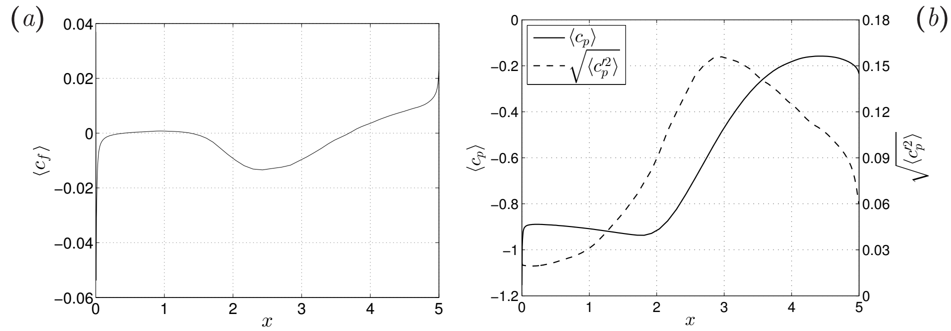


Figure 6: (a) Streamwise behaviour of the average skin friction coefficient $\langle c_f \rangle(x)$. (b) Streamwise evolution of the average pressure coefficient $\langle c_p \rangle(x)$ and of its standard deviation $\sqrt{\langle c_p'^2 \rangle}(x)$.

hence, the predicted extent of the recirculation regions. Accordingly, the present data should help to clarify the behaviour of mean and fluctuating pressure field at the wall, since they are not affected by turbulence modelling and mesh resolution issues.

Figure 6(b) shows that the mean pressure coefficient $\langle c_p \rangle(x)$ is always negative on the rectangular cylinder. It starts from its minimum at the leading-edge corner and shows a sharp increase in a very small region corresponding to the region of upstream reattachment of the *primary vortex*. Then, for $x > 0.13$, a weak decrease is observed up to $x \approx 1.81$. This streamwise location is the wall footprint of the low-pressure levels associated with the *primary vortex* core. Further downstream, the wall pressure shows a significant increase. This pressure rise is maintained up to $x \approx 4.39$ where it forms a maximum, since a slight pressure decrease follows up to the trailing edge corner.

As shown again in figure 6(b), the variance of the wall pressure fluctuations is very low in the very first part of the rectangular cylinder. However, a monotonic increase with the streamwise location is observed, leading to a maximum intensity for $x \approx 2.96$. Downstream this maximum, an almost equivalent decrease of the intensity of the wall pressure fluctuations is observed and maintained up to the trailing edge corner.

## 4. Single-point statistics

In figure 7, the behaviour of the turbulent intensities and of the fluctuating pressure is reported in the $(x, y)$-plane. These plots show that the separation at the leading-edge gives rise to a free-shear layer which is essentially laminar in its first portion. The instabilities associated with the shear layer are then amplified moving downstream and, for $x > 1$, a three dimensional turbulent pattern is observed. Indeed, all the three components of turbulence are different from zero. By following the streamline of the *primary vortex*, shown with dashed line in figure 7, it is evident that the most amplified fluctuations in the leading edge free shear layer are the streamwise ones, while the vertical and spanwise fluctuations are still significant but remain weaker.

Let us analyze in detail the behaviour of each component of turbulent fluctuation. By considering first the intensity of the streamwise fluctuations, figure 7(a), a well-defined region of maximum turbulent intensity can be identified. This region crosses the external paths of the average recirculating bubble for $1.5 < x < 3.5$ with a maximum reached at $(x, y) = (2.57, 0.44)$. The iso-levels of streamwise fluctuations are stretched in the streamwise direction. Apparently, no deflection of the isocontours towards the wall is observed, indicating that detached streamwise fluctuations are mostly convected from the *primary vortex* to the wake region without interacting with the wall. A second weaker region of streamwise fluctuations is observed in the wake with a relative maximum located at $(x, y) = (6.05, -0.05)$. The vertical location suggests that this relative maximum is a result of the amplification, throughout the trailing edge shear layer, of fluctuations produced in the attached forward boundary layer.

The vertical fluctuations show a substantially different behaviour with respect to the streamwise ones. As already mentioned, the typical intensity of vertical fluctuations is smaller than the streamwise ones. However, as shown in figure 7(b), significant differences are observed also from a topological point of view. The region of maximum intensity is located further downstream and closer to the wall with a maximum at $(x, y) = (2.96, 0.31)$. This aspect could be

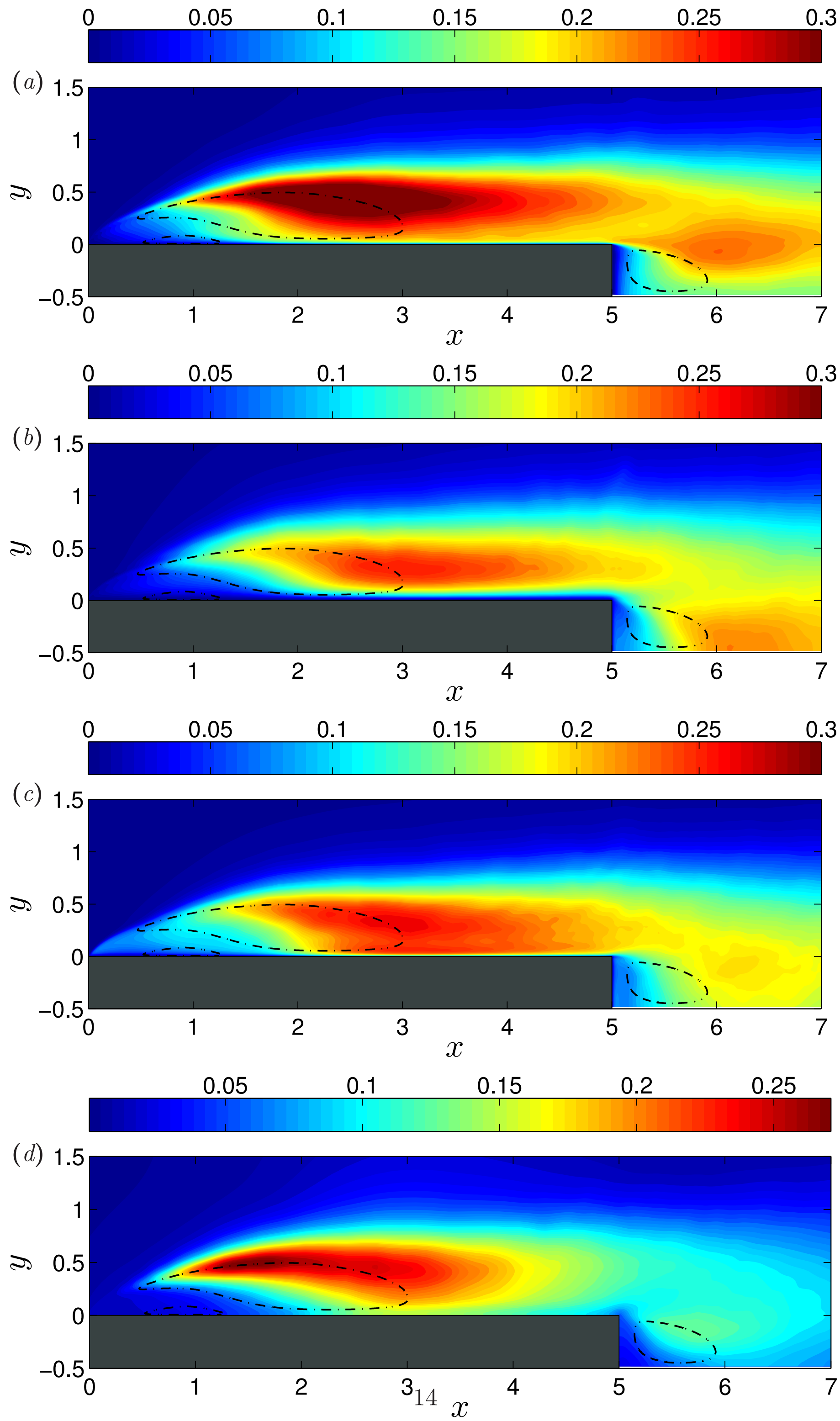




Figure 7: Isocontours of the turbulent intensities and of the fluctuating pressure in the $(x, y)$-plane: $\sqrt{\langle u'^2 \rangle}$, $\sqrt{\langle v'^2 \rangle}$, $\sqrt{\langle w'^2 \rangle}$ and $\sqrt{\langle p'^2 \rangle}$ in (a), (b), (c) and (d) respectively. The dashed lines report the location of the *primary vortex*, *secondary vortex* and *wake vortex*.

partially ascribed to the mean velocity paths associated with the downstream part of the *primary vortex*. Indeed, downstream the peak of intensity of the streamwise fluctuations, the mean velocity field bends towards the wall before reattaching. Hence, the structures associated with these intense streamwise fluctuations, being advected and stretched by the mean velocity field, undergo a deflection towards the wall thus leading to a partial reorientation of streamwise fluctuations in vertical ones. Also in this case, the shape of the isocontours of vertical fluctuations is found to be essentially elongated in the streamwise direction. Hence, as for the streamwise ones, the produced vertical fluctuations do not seem to interact with the wall, but rather they appear to be freely advected downstream towards the free flow. The second region of activity of vertical fluctuations occurs in the wake region. Contrarily to what happens for streamwise fluctuations, this region is centered in the symmetry plane of the wake at $y = -0.5$ for $x \approx 6.15$. This is a clear footprint of the periodic shedding of large scale vortices in the separated wake.

The most interesting aspect of the spanwise fluctuations shown in figure 7(c) is that the region of high turbulent intensity, located at $(x, y) = (2.96, 0.28)$ and associated with the *primary vortex*, extends also to the wall region and forms a thin layer of turbulent activity centered at $(x, y) = (2.96, 0.06)$. A possible explanation for the high intensity of spanwise fluctuations in the near-wall region is the following. Turbulent fluctuations produced through the *primary vortex* are, on average, transported towards the wall due to the deflection of the streamline paths of the mean velocity field. The consequent impingement gives rise to horizontal fluctuations, since the impermeability constraint of the wall leads to a dumping of the vertical fluctuations in the near-wall region. Actually, as shown here in quantitative terms, the impingement essentially gives rise to spanwise fluctuations. Indeed, we observe a near-wall layer in the reattachment region characterized by intense spanwise and weak streamwise fluctuations. From the reattachment region, a reverse flow takes origin, transporting turbulent fluctuations towards the leading-edge shear layer. Since the higher levels of turbulent intensities in the reattachment region are detected in the spanwise direction,

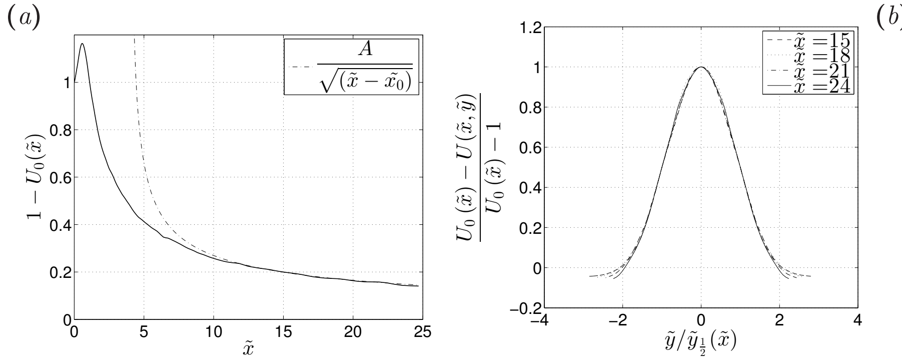


Figure 8: (a) Streamwise behaviour of the centerline velocity defect $1 - U_0(\tilde{x})$ (solid line). The self-similar power law decay (4) is reported in dashed line where $A = 0.66$ and $\tilde{x}_0 = 4$ are considered. (b) Vertical profiles of velocity defect $[U_0(\tilde{x}) - U(\tilde{x},\tilde{y})]/[U_0(\tilde{x}) - 1]$ evaluated at different streamwise locations and reported as function of $\tilde{y}/\tilde{y}_{1/2}(\tilde{x})$ where $\tilde{y}_{1/2}(\tilde{x})$ is the wake half-width defined such that $U(\tilde{x}, \pm\tilde{y}_{1/2}) = (1 + U_0)/2$.

these fluctuations result to be the most intense also in the reverse flow region, thus forming the observed near-wall layer of intense spanwise fluctuations.

Let us now analyse the behaviour of the fluctuating pressure field shown in figure 7(d). The most intense region of fluctuations is again the leading-edge shear layer and its consequent evolution along the *primary vortex*. In accordance with the behaviour of the pressure coefficient shown in figure 6(b), the region of reverse flow of the *primary vortex* is essentially unperturbed. Only for $x > 2$ the high levels of pressure fluctuations above the *primary vortex* are felt in the near-wall region. Interestingly, the variance of the pressure fluctuations associated with the vortex shedding in the separated wake forms a second region of activity, which however appears to be much weaker with respect to the region associated with the leading-edge shear layer.

To conclude this section, we consider the evolution of the wake also in the far field. For this analysis it is useful to consider a shifted reference frame $(\tilde{x}, \tilde{y}) = (x + 5D, y - D/2)$. In figure 8(a) the streamwise behaviour of the wake centerline velocity defect, $1 - U_0(\tilde{x})$ with $U_0(\tilde{x}) = U(\tilde{x}, 0)$, is shown. As

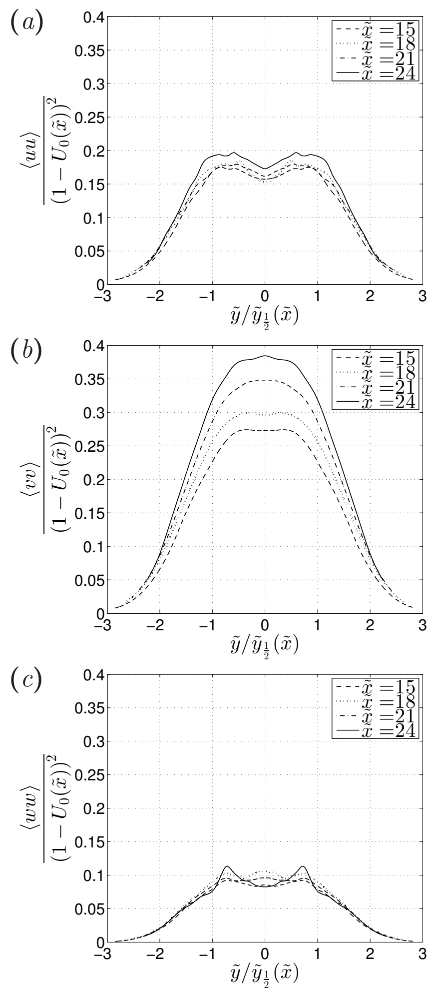


Figure 9: Vertical profiles of turbulent intensities evaluated at different streamwise locations and scaled in similarity variables. (a) streamwise, (b) vertical and (c) spanwise turbulent intensities.

apparent, the wake centerline velocity approaches the self-similar decay,

$$1 - U_0(\tilde{x}) \approx \frac{A}{\sqrt{\tilde{x} - \tilde{x}_0}} \tag{4}$$

for $\tilde{x} > 10$. The self-similarity of the mean streamwise velocity is confirmed in figure 8(b) where the vertical profiles of the velocity defect,

$$\frac{U_0(\tilde{x}) - U(\tilde{x}, \tilde{y})}{U_0(\tilde{x}) - 1} \tag{5}$$

evaluated at different streamwise locations for $\tilde{x} > 10$ are reported as a function of the similarity variable $\tilde{y}/\tilde{y}_{1/2}(\tilde{x})$ where $\tilde{y}_{1/2}(\tilde{x})$ is the wake half-width defined such that,

$$U(\tilde{x}, \pm\tilde{y}_{1/2}) = (1 + U_0)/2 \; . \tag{6}$$

It is worth noting that the above self-similar behaviour implies [22] that

$$\frac{1}{1 - U_0} \frac{d\tilde{y}_{1/2}}{d\tilde{x}} \approx const \tag{7}$$

and, hence, that the wake spreads as a power law, i.e. $\tilde{y}_{1/2} \sim \tilde{x}^{1/2}$.

To complete the analysis of the wake in the far field, let us analyse the behaviour of the turbulent intensities shown in figure 9. Similarity variables are again utilized and a good degree of scaling is observed for the streamwise and spanwise components of turbulent fluctuations. In contrast, the vertical fluctuations do not exhibit self-similarity, at least at the considered streamwise locations. This aspect denotes a slower asymptotic recovery of the equilibrium conditions needed for self-similarity, i.e. the vertical fluctuations are found to maintain memory of the shedding mechanisms of separating and reattaching flow over a longer distance.

## 5. The structure of turbulence and two-point statistics

In this section, the main unsteadiness of the flow and the inherent multiscale nature of the turbulent fluctuations are analysed by means of two-point statistics. Before that, we start by addressing the topological pattern taken by the main turbulent fluctuations populating the flow. To this aim we consider the eduction scheme proposed by Jeong *et al.* [23] and based on the second largest eigenvalue ($\lambda_2$) of the tensor

$$S_{ik}S_{kj} + \Omega_{ik}\Omega_{kj} \tag{8}$$

where

$$\begin{aligned} S_{ij} &= \frac{1}{2}\left(\frac{\partial u_i}{\partial x_j} + \frac{\partial u_j}{\partial x_i}\right) \\ \Omega_{ij} &= \frac{1}{2}\left(\frac{\partial u_i}{\partial x_j} - \frac{\partial u_j}{\partial x_i}\right) \end{aligned} \tag{9}$$

are the symmetric and antisymmetric part of the velocity gradient tensor. This eduction scheme is known to accurately extract the three-dimensional pattern of vortical structures, see e.g. Cucitore *et al.* [24] and Dubief *et al.* [25].

In figure 10, the instantaneous pattern taken by $\lambda_2 = -2$ is shown with iso-surfaces colored by $\tilde{y}$. From the perspective and top views, it is evident that in the very first part of the leading-edge shear layer, for $x < 0.3$, the flow is laminar, in accordance with the statistical analysis reported so far. Then, almost two-dimensional spanwise rolls appear as a result of the well-known Kelvin-Helmholtz instability. Under the effect of the mean shear, perturbations of the flow field lead to the lift up and stretching of these spanwise vortices, thus forming hairpin-like structures [6, 26, 27]. Hence, the flow motion develops streamwise vortices [19, 28, 29], the legs of the hairpin vortices, which in turn induce high- and low-speed streaks in between them. The statistical evidence of the presence of streamwise vortices and streaks is reported in the following analysis of the two-point spanwise correlation function. These sparsely distributed structures, grow, burst and decay thus giving rise to a fully turbulent flow for $x > 1$. Most of this complex multiscale pattern, particularly the large scale structures, is shed downstream in the free flow. On the other hand, a portion of the structures, in particular small scale fluctuations, are pushed towards the wall. The consequent impingement gives rise to both forward and reverse boundary layers characterized by small scale motions. By following the branch moving downstream, we observe that turbulent fluctuations become more and

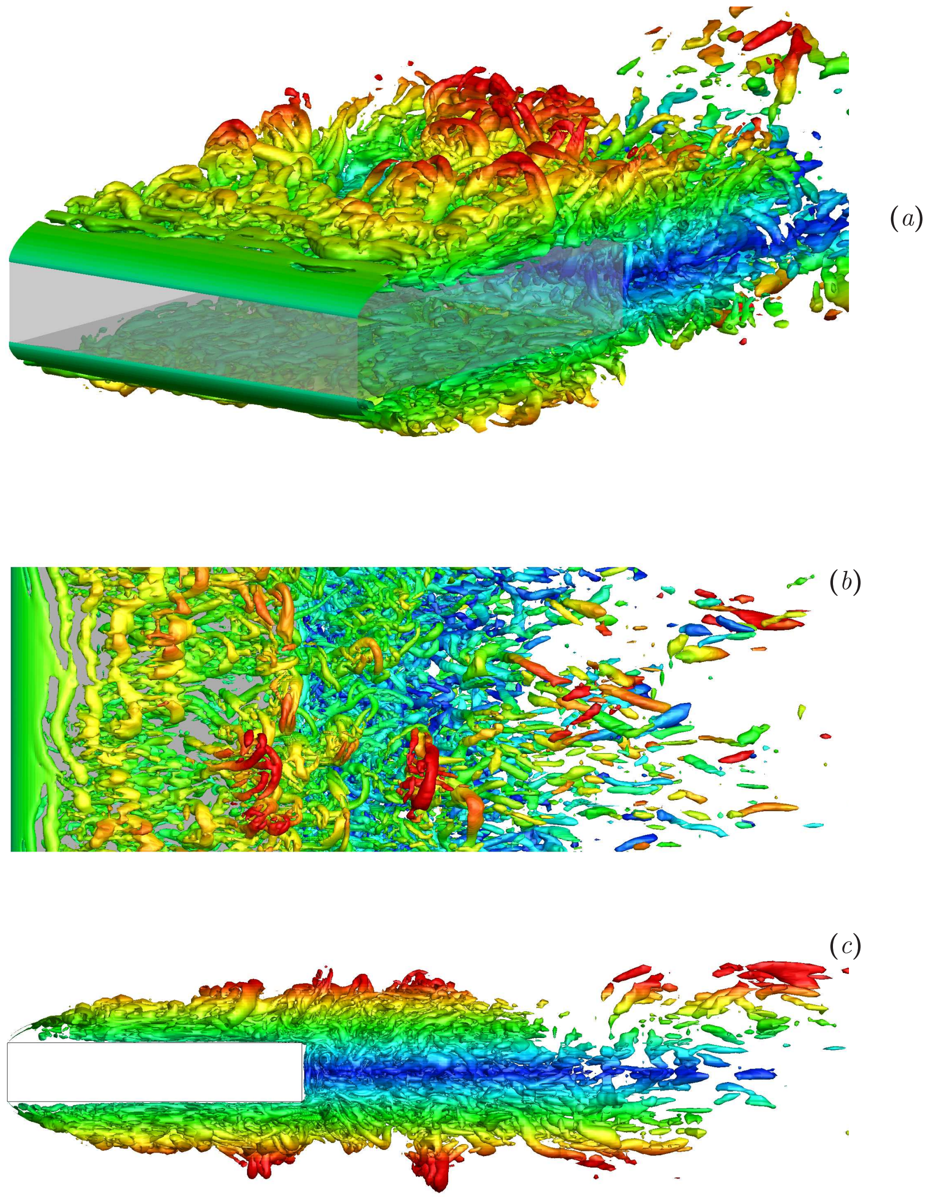


Figure 10: Instantaneous isosurfaces of $\lambda_2 = -2$ colored with $\tilde{y}$. Perspective, top and lateral views in (a), (b) and (c) plots, respectively.

more aligned in the streamwise direction. Finally, by reaching the trailing edge, these relatively small fluctuations are encompassed by an oscillatory large scale motion reminiscent of the laminar von Kármán instability of the separated wake.

The statistical signature of the above mentioned turbulent motion can be highlighted by means of two-point statistics, such as the correlation function in physical space and the energy spectrum in wavenumber/frequency space. While the spatial correlation function is a measure of how the velocity fluctuations are coherent in space, the energy spectrum allows us to analyse how turbulent kinetic energy is distributed across the different scales of motion. Let us start with the spatial correlation function. Due to the symmetry of the flow, the only statistical homogeneous direction where it is possible to define a space of homogeneous scales not affected by the inhomogeneity of the flow, is the spanwise direction (see Cimarelli *et al.* [30] for an example of the complexity emerging from the study of the space of inhomogeneous scales). In this setting, the spatial spanwise correlation function is rigorously defined and for a generic quantity $\beta$ can be written as,

$$R_{\beta\beta}(x,y,r_z) = \frac{\langle \beta'(x,y,z+r_z/2,t)\beta'(x,y,z-r_z/2,t)\rangle}{\langle \beta'\beta'\rangle(x,y)} \ . \tag{10}$$

In figure 11, the spanwise correlation function of the three components of velocity and pressure fluctuations evaluated in the shedding region of the *primary vortex*, is shown. This region of the flow is fully turbulent and relatively small spanwise correlation lengths are observed. In particular, the fluctuating velocity field shows a zero value of correlation at $r_z \approx 0.3$ for the vertical and streamwise fluctuations and at $r_z \approx 0.5$ for the spanwise ones. Interestingly, for larger values of the spanwise increment $r_z$, a degree of negative correlation is observed. The peak of anticorrelation occurs at $r_z \approx 0.45$, 0.5 and 0.9 for the vertical, streamwise and spanwise fluctuations, respectively. These negative correlation peaks are in accordance with the presence of streamwise vortices and streamwise velocity streaks as a result of motions induced by the hairpin vortices observed in figure 10. Indeed, the peak of negative correlation of vertical and spanwise fluctuations can be understood as a statistical evidence of

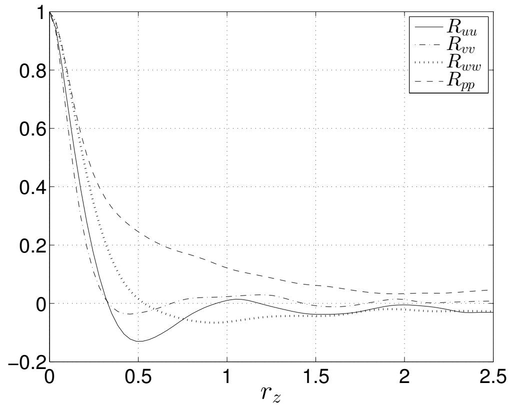


Figure 11: Spanwise correlation function of streamwise, vertical, spanwise and pressure fluctuations evaluated in the shedding region of the *primary vortex* at a $(x, y)$-position corresponding to probe 9. The specific location of the probe within the flow is shown in figure 4.

the presence of counter-rotating pairs of streamwise vortices. In particular, the negative peak of $R_{vv}$ at $r_z \approx 0.45$ is a measure of the statistical diameter of streamwise vortices while the negative peak of $R_{ww}$ at $r_z \approx 0.9$ is indicative of the mean spacing between counter-rotating vortex pairs. On the other hand, the negative peak of $R_{uu}$ is an evidence of the presence of streamwise velocity streaks. In particular, the negative peak of $R_{uu}$ at $r_z \approx 0.5$ is a measure of the mean spanwise spacing between high and low streamwise velocity streaks. See Kim *et al.* [31] for well-established and analogous considerations in wall-turbulent flows. The pressure fluctuations show a wider correlation length and no negative correlation peak is observed. Finally, it is worth pointing out that the behaviour shown here by the two-point spatial correlation function supports the choice of the numerical domain width, $\mathcal{D}_z = 5$. Indeed, figure 11 shows that the velocity and pressure fields are uncorrelated for spanwise lengths that are significantly shorter than the domain width.

Let us consider now the scale-space distribution of kinetic energy by means of a spectral analysis. In particular, we consider the multiscale features of the flow both in time and space by means of one-dimensional spectra of turbulent kinetic energy. By taking advantage of the statistical homogeneity of the flow in the spanwise direction and in time, the spectrum of turbulent kinetic energy $q = u_i u_i / 2$ can be defined as

$$\Phi_{qq}(k_z, St, x, y) = \frac{1}{2} \langle \tilde{u}_i(k_z, St, x, y) \tilde{u}_i^*(k_z, St, x, y) \rangle \tag{11}$$

where $k_z$ and $St$ are the spanwise wavenumber and frequency, while $\tilde{(\cdot)}$ denotes the two-dimensional Fourier transform with respect to the spanwise direction and time. To simplify the analysis, in the following we consider separately the one-dimensional wavenumber spectrum and the one-dimensional frequency spectrum. The one-dimensional wavenumber spectrum is derived from the two-dimensional one by integration with respect to $St$,

$$\Phi_{qq}^{k_z}(k_z, x, y) = \int \Phi_{qq}(k_z, St, x, y) dSt \tag{12}$$

and, analogously, the one-dimensional frequency spectrum is computed by integrating with respect to $k_z$,

$$\Phi_{qq}^{f}(St, x, y) = \int \Phi_{qq}(k_z, St, x, y) dk_z \tag{13}$$

By using the Taylor's hypothesis of frozen turbulence we also address the putative wavenumber spectrum in the streamwise direction defined as

$$\Phi_{qq}^{k_x}(k_x, x, y) = \Phi_{qq}^{f}(St/U(x, y), x, y) \ . \tag{14}$$

The main unsteadinesses of the flow are analysed in figure 12 by means of frequency spectra of turbulent kinetic energy evaluated in the leading-edge shear layer and in the wake. As shown in figure 12(a), the leading-edge shear layer is characterized by well-defined peaks of spectral energy at a relatively large range of frequencies. In particular, moving from probe P1 to P7 along the shear layer, the peaks move from $St \approx 1.8$ to $St \approx 0.9$. This range of frequencies represents the temporal scales of the fluctuations amplified by the transitional mechanisms of the shear layer. By looking at the frequency spectrum in the wake 12(b), a clear separation of scales is evinced between the vortex detachment in the separated wake and the amplified fluctuations through the leading-edge shear layer. In fact, the frequency spectrum in the wake highlights a well-defined peak at

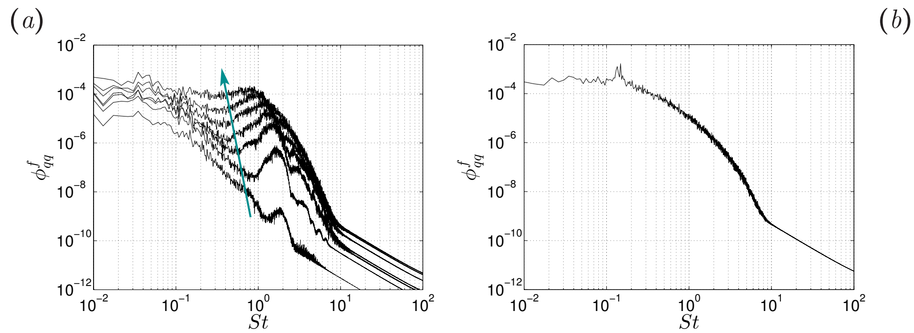


Figure 12: Frequency spectrum of turbulent kinetic energy, $\phi^f_{qq}(St)$, evaluated along the leading-edge shear layer at probes 1 to 7 (a) and in the wake at probe 10 (b). The arrow in (a) indicates probes from 1 to 7. The specific location of probes within the flow is shown in figure 4.

relatively larger temporal scales for $St \approx 0.14$. This peak is a clear statistical evidence of the oscillatory large scale motion reminiscent of the laminar von Kármán instability. Being at much larger temporal scales, the vortex shedding mechanisms in the wake are found to be not directly connected with the formation processes of fluctuations in the transitional region of the leading-edge shear layer. To appreciate this, one may compare the spectral peak at frequency $St \approx 0.14$ shown in figure 12(b) with the amplified spectral peak frequencies from $St \approx 1.8$ to $St \approx 0.9$ in figure 12(a). On the contrary, we find a clear matching of scales between the slow vortex detachment in the separated wake and the fluctuation of the lift coefficient, which appear evidently by comparing the spectral peaks for $St \approx 0.14$ in figures 3(b) and 12(b). Being driven by the pressure differences between the top and bottom sides of the rectangular cylinder, the temporal fluctuations of the lift coefficient are essentially given by the instantaneous difference in the extent of the low pressure regions settled by the separated recirculating flow in the opposite sides of the rectangle. Hence, we argue that the spectral peak frequency $St \approx 0.14$ shown by the lift coefficient is representative of the time scale of the large scale phenomenon of alternative enlargment and shrinking of the separation bubble in the top and bottom sides of the rectangle [18, 19]. Accordingly, the clear matching of scales between the

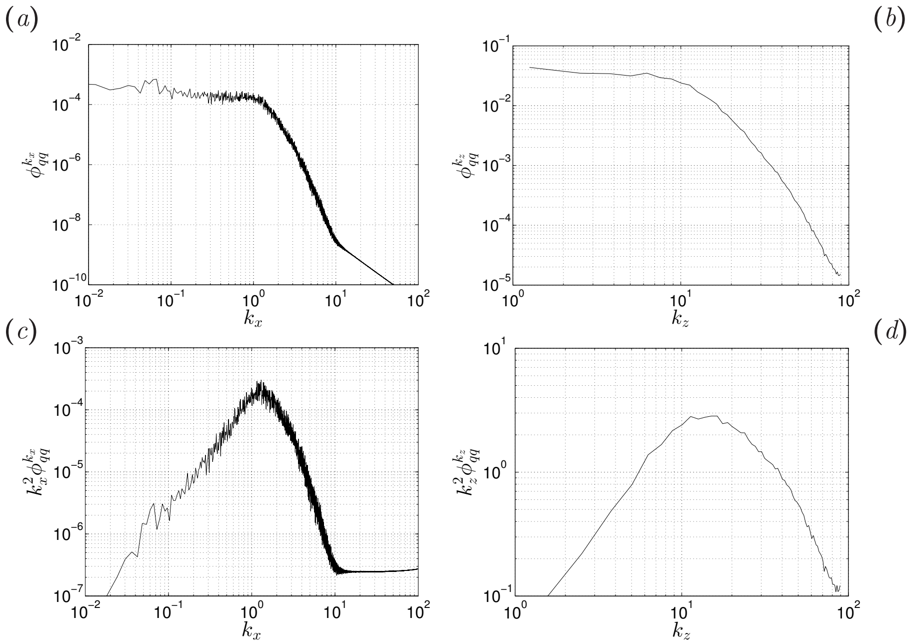


Figure 13: Streamwise (a) and spanwise (b) spectrum of turbulent kinetic energy, $\phi_{qq}^{k_x}(k_x)$ and $\phi_{qq}^{k_z}(k_z)$, respectively, evaluated at probe 8. Streamwise (c) and spanwise (d) dissipation spectrum of turbulent kinetic energy, $k_x^2\phi_{qq}^{k_x}(k_x)$ and $k_z^2\phi_{qq}^{k_z}(k_z)$, respectively, evaluated again at probe 8.

vortex detachment in the wake and the fluctuation of the lift coefficient suggests a locking of the vortex shedding phenomena in the wake with the alternative shedding of large scale vortices from the top and bottom *primary vortices* and, hence, with their enlargment and shrinking [2].

Let us consider now the spatial scales of the flow. In figure 13(a) and (b), the streamwise and spanwise spectra of turbulent kinetic energy in the fully developed part of the leading-edge shear layer are shown. The two plots reveal a markedly anisotropic behaviour, consisting of turbulent fluctuations elongated in the streamwise direction. Indeed, the energy-containing fluctuations are found to fill the streamwise spectrum up to $k_x \approx 1$ while, in the spanwise one, up to $k_z \approx 10$. In other words, the most energetic fluctuations are stretched in the streamwise direction and their size is of the order of $O(D)$ and $O(10^{-1}D)$ in the streamwise and spanwise direction, respectively. This anisotropy is retained up to the small dissipative scales as shown by the spectra of turbulent dissipation shown in figure 13(c) and (d). Indeed, the maximum rate of dissipation is achieved for $k_x \approx 1.4$ and $k_z \approx 15$, respectively in the streamwise and spanwise direction. These aspects need to be taken carefully into account when CFD techniques such as LES (Large Eddy Simulation) are applied for the simulation of the flow. Accordingly with Bruno *et al.* [32], the spanwise resolution is a central object when setting up a CFD simulation being the site of the smallest but energy containing scales of the flow as shown here in quantitative terms.

## 6. Conclusions

The flow around rectangular cylinders is recognized to be an extremely interesting case both for fundamental and applicative studies. Despite the simple geometry, this category of flows contains basic phenomena characterizing the behaviour of more complex flows typical of the applications. In this respect, it is still difficult to achieve reliable results both from a numerical and experimental point of view. The reason is the high sensitivity of the different phenomena driving the flow on the experimental conditions from one side and on the turbulence modelling and mesh properties from the other. Here, we report for the first time a Direct Numerical Simulation of such a flow for a moderately high Reynolds number. The main goal is to shed light on the main physical mechanisms driving the complex behaviour of the flow and to provide well converged statistics not affected by uncertainties on the boundary conditions and by inaccuracies related to turbulence modelling and mesh resolution.

Global and single-point statistics are reported aiming at defining the exact behaviour of relevant statistical quantities. As an example, we characterize the behaviour of the pressure coefficient and of its variance which are known to be very important quantities for civil engineering applications aiming at predicting wind loads over buildings. In this respect, also the behaviour of the lift coefficient in the frequency space is reported, highlighting a well defined peak for $St \approx 0.14$. The mean and turbulent flow is then assessed. Three main recirculating regions are found and their dimensions and turbulence levels are characterized. The first one is a large scale bubble originating from the flow separation at the leading edge corner and it is herein called *primary vortex*. The related shear layer is the locus of the instability and transitional processes giving rise to turbulence as shown here in quantitative terms by the increasing levels of intensity of the fluctuations along its development. This *primary vortex* is found to shed vortices downstream giving rise to a region of high turbulence levels. The *primary vortex* is responsible for the observed second recirculating region, here called *secondary vortex*. Indeed, it induces a reverse flow at the wall which experiences an adverse pressure gradient and thus separates giving rise to the second near-wall recirculating region. Finally, the third recirculating region, here called *wake vortex*, takes place in the separated flow at the trailing edge. As for the *primary vortex*, the trailing-edge shear layer is responsible for additional instability mechanisms, thus giving rise to a second region of high turbulence intensity. Finally, the behaviour of the fully developed wake is also analysed. A rigorous assessment of the wake flow features is reported in a simple way by making use of self-similarity variables. The analysis reveals a slower asymptotic recovery of the equilibrium conditions for self-similarity of the vertical fluctuations with respect to the streamwise and spanwise ones.

To complete the study of the flow, two-point statistics are also computed, namely the spanwise correlation function and the energy spectrum. The study of the two-point spatial correlation function of the fluctuating velocity and pressure fields allows us first to prove that the width of the numerical domain is large enough to reproduce the main flow features. On the other hand, we found a clear statistical evidence of the presence of streamwise vortices and high- and low- streamwise streaks within the flow. In particular, we found that streamwise vortices statistically occur as pairs of counter-rotating vortices. The spacing between counter-rotating vortex pairs is 0.9 while the diameter of a single streamwise vortex is 0.45. Regarding the velocity streaks we statistically prove their presence and we measure that the spanwise spacing between postive and negative streamwise velocity streaks is 0.9. We argue that both streamwise vortices and streaks are a result of the flow motion induced by the presence of hairpin-like turbulent structures here detected by analysing the instantaneous pattern taken by $\lambda_2$.

The spectral analysis in the frequency space allows us to identify and quantify the main unsteadinesses of the flow. In particular, a separation of scales between the amplified fluctuations in the leading-edge shear layer for $St = O(10^0)$ and the large scale vortex detachment at the wake for $St = O(10^{-1})$ is observed. Indeed, this low frequency is found to be actually locked with the shedding of vortices from the *primary vortex* and, in particular, with the alternative enlargment and shrinking of the recirculating regions in the top and bottom sides of the rectangle. On the other hand, the analysis in the wavenumber space allows us to study the anisotropy of the flow in the space of scales. It is found that both the energy-containing and dissipative fluctuations are anisotropic, being elongated in the streamwise direction and thin in the spanwise one. This information should be taken carefully into account when designing meshes in CFD applications.

It is finally worth pointing out that the present results, besides reporting a detailed statistical analysis of the flow, are also intended to be a reference for CFD studies. Indeed, the statistical objects here reported would be useful to quantify and understand the effects of modelling and mesh resolution issues by means of a comparison with the same statistics obtained with CFD simulations at the same Reynolds number. Hence, they would be useful for developing a *best practice* for CFD.

## References

[1] T. Tamura, T. Miyagi, T. Kitagishi, Numerical prediction of unsteady pressures on a square cylinder with various corner shapes, J. Wind Eng. Ind. Aerodyn. 74 (1998) 531–542.

[2] N. J. Cherry, R. Hillier, M. E. M. Latour, Unsteady measurements in a separated and reattaching flow., J. Fluid Mech. 144 (1984) 13–46.

[3] L. Bruno, M. V. Salvetti, F. Ricciardelli, Benchmark on the aerodynamics of a rectangular 5:1 cylinder: an overview after the first four years of activity, J. Wind Eng. Ind. Aerodyn. 126 (2014) 87–106.

[4] Y. Nakamura, Y. Ohya, S. Ozono, R. Nakamaya, Experimental and numerical analysis of vortex shedding from elongated rectangular cylinders at low Reynolds numbers 200–1000, J. Wind Eng. Ind. Aerodyn. 65 (1996) 301–308.

[5] Y. Ohya, Y. Nakamura, S. Ozono, H. Tsuruta, R. Nakayama, A numerical study of vortex shedding from flat plates with square leading and trailing edges, J. Fluid Mech. 236 (1992) 445–460.

[6] K. Hourigan, M. C. Thompson, B. T. Tan, Self-sustained oscillations in flows around long blunt plates, J. Fluids Struct. 15 (2001) 387–398.

[7] B. T. Tan, M. C. Thompson, K. Hourigan, Flow past rectangular cylinders: receptivity to transverse forcing, J. Fluid Mech. 515 (2004) 33–62.

[8] K. Shimada, T. Ishihara, Application of a modified k–$\varepsilon$ model to the prediction of aerodynamic characteristics of rectangular cross-section cylinders, J. Fluid Struct. 16 (4) (2002) 465–485.

[9] D. Yu, A. Kareem, Parametric study of flow around rectangular prisms using LES, J. Wind Eng. Ind. Aerodyn. 77 (1998) 653–662.

[10] G. Bartoli, L. Bruno, G. Buresti, F. Ricciardelli, M. Salvetti, A. Zasso, Barc overview document, See http://www. aniv-iawe. org/barc for further details (accessed 27/08/2011).

[11] L. Bruno, D. Fransos, N. Coste, A. Bosco, 3D flow around a rectangular cylinder: a computational study, J. Wind Eng. Ind. Aerodyn. 98 (2010) 263–276.

[12] C. Mannini, A. Šoda, G. Schewe, Numerical investigation on the three-dimensional unsteady flow past a 5:1 rectangular cylinder, J. Wind Eng. Ind. Aerodyn. 99 (2011) 469–482.

[13] M. Ricci, L. Patruno, S. de Miranda, F. Ubertini, Flow field around a 5: 1 rectangular cylinder using LES: Influence of inflow turbulence conditions, spanwise domain size and their interaction, Comput. Fluids 149 (2017) 181–193.

[14] L. Patruno, M. Ricci, S. de Miranda, F. Ubertini, Numerical simulation of a 5:1 rectangular cylinder at non-null angles of attack, J. Wind Eng. Ind. Aerodyn. 151 (2016) 146–157.

[15] T. Tamura, Y. Itoh, K. Kuwahara, Computational separated-reattaching flows around a rectangular cylinder, J. Wind Eng. Ind. Aerodyn. 50 (1993) 9–18.

[16] K. Sasaki, M. Kiya, Three-dimensional vortex structure in a leading-edge separation bubble at moderate Reynolds numbers, J. Fluids Eng. 113 (3) (1991) 405–410.

[17] Y. Nakamura, Y. Ohya, H. Tsuruta, Experiments on vortex shedding from flat plates with square leading and trailing edges, J. Fluid Mech. 222 (1991) 437–447.

[18] M. Kiya, K. Sasaki, Structure of a turbulent separation bubble, J. Fluid Mech. 137 (1983) 83–113.

[19] M. Kiya, K. Sasaki, Structure of large-scale vortices and unsteady reverse flow in the reattaching zone of a turbulent separation bubble, J. Fluid Mech. 154 (1985) 463–491.

[20] H. Weller, G. Tabor, H. Jasak, C. Fureby, A tensorial approach to computational continuum mechanics using object-oriented techniques, Computers in physics 12 (6) (1998) 620–631.

[21] R. Issa, Solution of the implicitly discretised fluid flow equations by operator-splitting, J. Comput. Phys. 62 (1) (1986) 40–65.

[22] S. B. Pope, Turbulent flows (2001).

[23] J. Jeong, F. Hussain, W. Schoppa, J. Kim, Coherent structures near the wall in a turbulent channel flow, J. Fluid Mech. 332 (1997) 185–214.

[24] R. Cucitore, M. Quadrio, A. Baron, On the effectiveness and limitations of local criteria for the identification of a vortex, Eur. J. Mech. B/Fluids 18 (2) (1999) 261–282.

[25] Y. Dubief, F. Delcayre, On coherent-vortex identification in turbulence, J. Turbulence 1 (1) (2000) 011–011.

[26] M. Langari, Z. Yang, Numerical study of the primary instability in a separated boundary layer transition under elevated free-stream turbulence, Phys. Fluids 25 (2013) 074106.

[27] C. Tenaud, B. Podvin, Y. Fraigneau, V. Daru, On wall pressure fluctuations and their coupling with vortex dynamics in a separated–reattached turbulent flow over a blunt flat plate, Int. J. Heat Fluid Flow 61 (2016) 730–748.

[28] L. P. Bernal, A. Roshko, Streamwise vortex structures in plane mixing layers, J. Fluid Mech. 170 (1986) 499–525.

[29] J. Jiménez, A spanwise structure in the plane shear layer, J. Fluid Mech. 132 (1983) 319–336.

[30] A. Cimarelli, E. De Angelis, J. Jiménez, C. Casciola, Cascades and wall-normal fluxes in turbulent channel flows, J. Fluid Mech. 796 (2016) 417436.

[31] J. Kim, P. Moin, R. Moser, Turbulence statistics in fully developed channel flow at low Reynolds number, J. Fluid Mech. 177 (1987) 133–166.

[32] L. Bruno, N. Coste, D. Fransos, Simulated flow around a rectangular 5:1 cylinder: spanwise discretization effects and emerging flow features, J. Wind Eng. Ind. Aerodyn. 104 (2012) 203–215.